A Novel Approach to Full-Polarimetric Short-Range Imaging with Co-polarized Data

Wang, Jianping; Aubry, Pascal; Yarovyi, Olexander

DOI
10.1109/TAP.2016.2610102

Publication date
2016

Document Version
Accepted author manuscript

Published in
IEEE Transactions on Antennas and Propagation

A Novel Approach to Full-Polarimetric Short-Range Imaging with Co-polarized Data

Jianping Wang, Pascal Aubry and Alexander Yarovoy, *Fellow, IEEE*

***Abstract*—A novel approach to full-polarimetric short-range imaging with rotating arrays is proposed. Instead of taking advantage of all four possible combinations of the polarizations of transmit and receive antennas as in the typical full-polarimetric imaging systems, the suggested antenna array acquires three different co-polarized measurements at each spatial sampling point with its rotation. A simple algebraic operation is derived to accurately retrieve the full-polarimetric signals in the H/V polarization basis from the co-polarized measurements. After the retrieval of the full-polarimetric signals, the traditional imaging algorithms can be applied to reconstruct the polarimetric images. The effectiveness and accuracy of the suggested approach to full-polarimetric imaging are validated on the signal and image levels through both numerical simulations and experiments. The results show that the proposed approach can accurately retrieve the full-polarimetric signals and provides an alternative method to signal acquisition for full-polarimetric imaging.**

***Index Terms*—Co-polarized data, Full-polarimetric imaging, Rotating array, Signal retrieve, Ultrawideband (UWB).**

I. Introduction

DUE to the combination of penetration capabilities with reasonable cross-range resolution, microwave imaging is widely used nowadays in numerous applications in remote sensing, ground penetrating radar, security check, medical imaging, etc [1]–[5]. Taking advantage of real or synthetic antenna array with electrically large aperture and wideband signals, microwave imaging systems possess high resolving capabilities in both cross-range and down-range directions, which are similar to many scalar wave imaging systems, for example, acoustic imaging systems [6]. However, electromagnetic wave is a vector wave which is distinct and significant feature in the contrast to scalar waves. Due to this vectorial nature of electromagnetic waves, the acquired signals scattered from targets show marked dependence on the transmit and receive antenna polarizations. So exploiting the polarization diversity could bring extra benefits for the extraction of the scattering properties of target reflectors.

Numerous polarimetric imaging systems have been developed for (synthetic aperture) radars to exploit the vectorial characteristics of electromagnetic wave and improve both detectability and classification of targets [7]–[22]. Typically, the polarimetric imaging systems record multi-components of the electromagnetic waves through different polarization combinations of transmit and receive antennas. Dual-polarized radar system acquires two differently polarized signals scattered from targets by using single linear (say, H- or V-) polarized transmitter and dual-polarized (H- and V-) polarized receiver, or dual polarized transmitter and single polarized receiver. Application of dual-polarized antennas for both transmission and receiving leads to quad-polarized radar. One should note that these dual-polarized and quad-polarized radar systems are generally designed such that the receiver polarization basis agrees with the transmitted basis. This kind of quad-polarized signal acquisition strategy has been used for both remote sensing and short range applications [7]–[15]. After obtaining the full-polarimetric (usually HH, HV, VH and VV) signals through the four polarization combinations of transmit and receive antennas, each polarimetric signal is typically processed individually to form an image with the imaging algorithms developed under the scalar wave assumption and then polarization decomposition techniques are applied to the focused polarimetric images to extract the size, shape, orientation and other scattering features of targets. In contrary to this typical approach, van der Kruk et al [16] presented a multi-component imaging approach that jointly migrate the co-polarized and cross-polarized signals as a matrix and thus all the information of co-pol and cross-pol signals is merged in one image. For short-range applications, such as Ground Penetrating Radar (GPR) such an approach provides improved results in comparison to the traditional one. In addition, combining the spatial diversity of antenna arrays, full-polarimetric MIMO radar systems have been studied and developed for GPR applications [17]–[19].

Sometimes due to the limited system resources (power, mass, available space, cost, etc), quad-polarized radar is not realizable but the polarimetric information of targets is still desirable to be extracted. Thus compact polarimetry was proposed and developed by exploiting different polarization bases for transmission and receive to still realize benefits of the traditional quad-polarized radar measurements. Souyis et al [20] suggested a compact-polarized configuration, i.e., $\pi/4$ mode for SAR imaging, where the antennas radiate the electric field at 45 with respect to H and V orientations and then the H and V components of the scattered signals are coherently received. Based on the various hypotheses on the symmetry properties of geophysical media in the scene of interest, the $\pi/4$ mode provides potential to reconstruct the full polarimetric information of extended targets. In [21], Raney extended the concept of $\pi/4$ by replacing the linear-polarized transmission with circular-polarized transmission, i.e., circular transmit, linear receive, named as hybrid-polarity architecture. Its rotation-invariant properties of illumination

This research is supported by the NeTTUN project funded by European Commission within the FP-7 framework under the grant of 280712.

J. Wang, P Aubry and A. Yarovoy are with Faculty of Electrical Engineering, Mathematics and Computer Science (EEMCS), Delft University of Technology, 2628CD Delft, the Netherlands e-mail: J.Wang-4@tudelft.nl, P.J.Aubry@tudelft.nl, A.Yarovoy@tudelft.nl.

make it an appealing choice for some significant applications, e.g., planetary geology, in which the dihedral-like scattering features should be classified via decomposition regardless of their orientations. Actually both $\pi/4$ mode and hybrid-polarity architecture can be dated back to meteorological radars [22].

Although the compact polarimetry allows transmit and receive antennas to work at different polarization bases, it shares the same requirement with traditional full-polarimetric radars that the antennas have to maintain their polarization within the aperture during the measurements so as to get the same kind of polarized signals with respect to targets. However, this requirement is undesirable or even impractical in some circumstances, for example, the GPR systems used in the tunnel boring machines (TBM) where the antenna array is synthesized by the rotation of several antennas mounted on the cutter-head plane [23]–[25]. With the rotation of the cutter-head of TBM, the orientations (polarizations) of antennas are constantly changing. Thus, it is apparent that the signals scattered from targets are acquired in various polarization bases at different spatial positions within the synthetic aperture. So the scalar wave based imaging algorithms [26], [27] as well as the matrix-inversion based reconstruction approach [16] are no longer explicitly applicable. Although the circular rotating sampling is utilized in [28], [29], the influence of antenna polarization variation during the measurement is ignored.

In this paper we investigate the effect of rotated polarizations of antennas on the recorded signals during the scattering process and propose an approach for full-polarimetric imaging using rotating arrays. The suggested rotating array collects three co-polarized measurements and then a simple algebraic operation is taken to retrieve the full-polarimetric signals in the H/V polarization basis. So it circumvents the constraint of the applicability of traditional imaging algorithms for full-polarimetric feature extraction.

The paper is organized as follows. In Section II, the scattering formalism is briefly reviewed. The wavefield extrapolator for rotated antenna is discussed in section III . An approach to design rotating array for full-polarimetric imaging is proposed in the same section. Section IV shows an array design example for the application of the proposed approach. Then in Section V and VI the effectiveness and accuracy of the rotating array for full-polarimetric imaging are demonstrated through numerical simulations and experiments. Finally, conclusions are drawn in Section VII.

II. Scattering Formulation

In this paper, the monostatic radar configuration is considered. We assume the antennas are deployed on the x_1-x_2 plane, and x_3 axis points towards the observation scenario and forms a right-hand coordinate system. Based on the Born approximation, the scattering process can be represented by a linear expression [16]

$$E^s_{\alpha\beta}\left(\mathbf{x}^R,\mathbf{x}^T,\omega\right) = \int_{V(\mathbf{x}^c)} D_{\alpha\beta}\left(\mathbf{x}^R,\mathbf{x}^T\middle|\,\mathbf{x}^c,\omega\right)\chi\left(\mathbf{x}^c\right)J_\beta\left(\mathbf{x}^T,\omega\right)\mathrm{d}\,V \quad (1)$$

where $\omega = 2\pi f$ is the angular frequency and $\mathbf{x} = (x_1, x_2, x_3)$ is the spatial coordinates. Superscripts R and T refer to the receive and transmit antennas while subscripts α and β take values $\{1, 2\}$ and represent, respectively, the receive and transmit antennas' orientations along the x_1 or x_2. $\chi\left(\mathbf{x}^c\right)$ is the contrast function at position $\mathbf{x}^c$, $J_\beta\left(\mathbf{x}^T,\omega\right)$ is the point source located at the position $\mathbf{x}^T$, and $D_{\alpha\beta}\left(\mathbf{x}^R,\mathbf{x}^T\middle|\,\mathbf{x}^c,\omega\right)$ is the forward wave extrapolator from the transmit antenna at $\mathbf{x}^T$ to the scatter at $\mathbf{x}^c$ and then to the receive antenna at $\mathbf{x}^R$. The contrast function χ is defined as $\chi\left(\mathbf{x}^c\right) = \hat{\eta}^s - \hat{\eta}$, which is the difference of the physical properties of the scatter $\hat{\eta}^s$ and background $\hat{\eta}$. The physical property $\hat{\eta}$ is defined as $\hat{\eta} = \sigma + j\omega\varepsilon$, where $j = \sqrt{-1}$, σ is the conductivity, ε is the permittivity. The point source $J_\beta\left(\mathbf{x}^T,\omega\right)$ can be denoted as

$$J_\beta\left(\mathbf{x}^T,\omega\right) = S\left(\omega\right)b_\beta\left(\mathbf{x}^T\right) \quad (2)$$

where $S\left(\omega\right)$ is the source wavelet radiated by source antenna and b_β indicates its orientation along x_1- or x_2-direction. The forward wavefield extrapolator $D_{\alpha\beta}\left(\mathbf{x}^R,\mathbf{x}^T,\omega\right)$ is defined by an inner product

$$D_{\alpha\beta}\left(\mathbf{x}^R,\mathbf{x}^T\middle|\,\mathbf{x}^c,\omega\right) = G_{\alpha\ell}\left(\mathbf{x}^R\middle|\,\mathbf{x}^c,\omega\right)G_{\ell\beta}\left(\mathbf{x}^c\middle|\,\mathbf{x}^T,\omega\right) \quad (3)$$

where $\ell \in \{1, 2, 3\}$ denotes the electric field directions. The Green's function $G_{\ell\beta}\left(\mathbf{x}^c\middle|\,\mathbf{x}^T,\omega\right)$ describes the propagation of electromagnetic wave from the source at position $\mathbf{x}^T$ to the scatterer at position $\mathbf{x}^c$ and the Green's function $G_{\alpha\ell}\left(\mathbf{x}^R\middle|\,\mathbf{x}^c,\omega\right)$ expresses the propagation from the scatterer at position $\mathbf{x}^c$ to the receive antenna at position $\mathbf{x}^R$. The forward wavefield extrapolator shown in (3) describes the scattering process with x_β oriented transmit antenna and x_α-oriented receive antenna. Hence (1) gives the scattered wave from illuminated volume received with x_α-oriented receive antenna related to the x_β oriented transmission. Accounting for a pair of orthogonal orientations of the receive antennas on the acquisition plane, the observed waves in the two directions can be arranged as a vector

$$\begin{bmatrix} E^s_1\left(\mathbf{x}^R,\mathbf{x}^T,\omega\right) \\ E^s_2\left(\mathbf{x}^R,\mathbf{x}^T,\omega\right) \end{bmatrix} = S\left(\omega\right) \cdot \int_{V(\mathbf{x}^c)} \mathbf{D}\left(\mathbf{x}^R,\mathbf{x}^T\middle|\,\mathbf{x}^c,\omega\right)\begin{bmatrix} b_1\left(\mathbf{x}^T\right) \\ b_2\left(\mathbf{x}^T\right) \end{bmatrix}\chi\left(\mathbf{x}^c\right)\mathrm{d}\,V \quad (4)$$

where $\begin{bmatrix} E^s_1 & E^s_2 \end{bmatrix}^\intercal$ is a measured vector by two received antennas with orthogonal orientations corresponding to two orthogonally polarized transmission, and here superscript $^\intercal$ refers to matrix transpose operation. It is given by

$$\begin{bmatrix} E^s_1\left(\mathbf{x}^R,\mathbf{x}^T,\omega\right) \\ E^s_2\left(\mathbf{x}^R,\mathbf{x}^T,\omega\right) \end{bmatrix} = \begin{bmatrix} E^s_{11}\left(\mathbf{x}^R,\mathbf{x}^T,\omega\right) + E^s_{12}\left(\mathbf{x}^R,\mathbf{x}^T,\omega\right) \\ E^s_{21}\left(\mathbf{x}^R,\mathbf{x}^T,\omega\right) + E^s_{22}\left(\mathbf{x}^R,\mathbf{x}^T,\omega\right) \end{bmatrix} \quad (5)$$

and $\mathbf{D}$ represents the forward wavefield extrapolator that is given by

$$\mathbf{D} = \begin{bmatrix} D_{11}\left(\mathbf{x}^R,\mathbf{x}^T\middle|\,\mathbf{x}^c,\omega\right) & D_{12}\left(\mathbf{x}^R,\mathbf{x}^T\middle|\,\mathbf{x}^c,\omega\right) \\ D_{21}\left(\mathbf{x}^R,\mathbf{x}^T\middle|\,\mathbf{x}^c,\omega\right) & D_{22}\left(\mathbf{x}^R,\mathbf{x}^T\middle|\,\mathbf{x}^c,\omega\right) \end{bmatrix} = \begin{bmatrix} G^R_{11} & G^R_{21} & G^R_{31} \\ G^R_{12} & G^R_{22} & G^R_{32} \end{bmatrix}\begin{bmatrix} G^T_{11} & G^T_{12} \\ G^T_{21} & G^T_{22} \\ G^T_{31} & G^T_{32} \end{bmatrix} \quad (6)$$

where G^R is short for $G^R\left(\mathbf{x}^R|\mathbf{x}^c,\omega\right)$ and G^T for $G^T\left(\mathbf{x}^c|\mathbf{x}^T,\omega\right)$. As we focus on the monostatic configuration in the paper, so for each observation transmit and receive antennas are located at the same position $\mathbf{x}^A$, i.e., $\mathbf{x}^T = \mathbf{x}^R = \mathbf{x}^A$. Therefore, Green's functions of transmit and receive antennas are equal in the corresponding electric field directions. Meanwhile, using the reciprocity properties of propagation, the elements of $\mathbf{D}$ can be explicitly written as

$$\begin{cases} D_{11} = G_{11}^2 + G_{21}^2 + G_{31}^2 \\ D_{12} = G_{11}G_{12} + G_{21}G_{22} + G_{31}G_{32} \\ D_{21} = G_{11}G_{12} + G_{21}G_{22} + G_{31}G_{32} \\ D_{22} = G_{12}^2 + G_{22}^2 + G_{32}^2 \end{cases} \tag{7}$$

where the Green's functions G are functions of $\mathbf{x}^c$, $\mathbf{x}^A$ and ω. From (7), it can be observed that in monostatic configuration D_{12} equals to D_{21}, which is the result of the reciprocity theorem.

III. Wavefield Extrapolator for Rotated Antennas

The variation of the orientations of transmit/receive antennas changes the polarizations of the radiated/received electromagnetic fields. In the monostatic configuration, simultaneously rotating the orientations of the transmit and receive antennas equivalently rotates the polarization coordinate system of the acquisition. Assume the new polarization coordinate system is rotated of an angle θ in clockwise direction with respect to the original one (e.g., (b_1, b_2) basis), then the received signal in the new polarization basis can be related to the measurements before rotation at the same position through the rotation matrix

$$\begin{aligned} \begin{bmatrix} E_1^s\left(\mathbf{x}^R,\mathbf{x}^T,\omega\right) \\ E_2^s\left(\mathbf{x}^R,\mathbf{x}^T,\omega\right) \end{bmatrix} &= R \begin{bmatrix} E_\theta^s\left(\mathbf{x}^R,\mathbf{x}^T,\omega\right) \\ E_{\theta_\perp}^s\left(\mathbf{x}^R,\mathbf{x}^T,\omega\right) \end{bmatrix} \\ \begin{bmatrix} b_1\left(\mathbf{x}^T\right) \\ b_2\left(\mathbf{x}^T\right) \end{bmatrix} &= R \begin{bmatrix} b_\theta\left(\mathbf{x}^T\right) \\ b_{\theta\perp}\left(\mathbf{x}^T\right) \end{bmatrix} \end{aligned} \tag{8}$$

where R is the rotation matrix and is expressed as

$$R = \begin{bmatrix} \cos\theta & \sin\theta \\ -\sin\theta & \cos\theta \end{bmatrix} \tag{9}$$

Inserting (8) into (4) and taking a simple algebraic manipulation result in

$$\begin{aligned} &\begin{bmatrix} E_\theta^s\left(\mathbf{x}^R,\mathbf{x}^T,\omega\right) \\ E_{\theta_\perp}^s\left(\mathbf{x}^R,\mathbf{x}^T,\omega\right) \end{bmatrix} = S(\omega) \\ &\cdot \int_{V(\mathbf{x}^c)} R^{-1}\mathbf{D}\left(\mathbf{x}^R,\mathbf{x}^T\middle|\,\mathbf{x}^c,\omega\right) R \begin{bmatrix} b_\theta\left(\mathbf{x}^T\right) \\ b_{\theta_\perp}\left(\mathbf{x}^T\right) \end{bmatrix} \chi\left(\mathbf{x}^c\right) \mathrm{d}\, V \end{aligned} \tag{10}$$

where R^{-1} is the inverse matrix of R. (10) formulates the scattering process in the polarization basis $(\theta, \theta_\perp)$. Compared to (4), in the polarization basis $(\theta, \theta_\perp)$ the forward wavefield extrapolator, denoted by $\hat{\mathbf{D}}$, can be defined as

$$\hat{\mathbf{D}} = R^{-1}\mathbf{D}\left(\mathbf{x}^R,\mathbf{x}^T\middle|\,\mathbf{x}^c,\omega\right) R \tag{11}$$

Equation (11) describes the relation of the forward wavefield extrapolators in two different polarization bases (b_1, b_2) and $(\theta, \theta_\perp)$. Substituting (9) for R, $\hat{\mathbf{D}}$ can be explicitly written as

$$\hat{\mathbf{D}} = \begin{bmatrix} \hat{D}_{11} & \hat{D}_{12} \\ \hat{D}_{21} & \hat{D}_{22} \end{bmatrix} \tag{12}$$

where

$$\begin{cases} \hat{D}_{11} = \cos^2\theta D_{11} - \sin\theta\cos\theta D_{21} \\ \qquad -\sin\theta\cos\theta D_{12} + \sin^2\theta D_{22} \\ \hat{D}_{12} = \sin\theta\cos\theta D_{11} - \sin^2\theta D_{21} \\ \qquad +\cos^2\theta D_{12} - \sin\theta\cos\theta D_{22} \\ \hat{D}_{21} = \sin\theta\cos\theta D_{11} + \cos^2\theta D_{21} \\ \qquad -\sin^2\theta D_{12} - \sin\theta\cos\theta D_{22} \\ \hat{D}_{22} = \sin^2\theta D_{11} + \sin\theta\cos\theta D_{21} \\ \qquad +\sin\theta\cos\theta D_{12} + \cos^2\theta D_{22} \end{cases} \tag{13}$$

For practical applications, two orthogonal oriented transmit antennas usually operate separately in time, and two orthogonal components are collected for each transmitted signal. This operation can be represented by setting the vector $\begin{bmatrix} b_\theta\left(\mathbf{x}^T\right) & b_{\theta_\perp}\left(\mathbf{x}^T\right) \end{bmatrix}^\intercal$ as $\begin{bmatrix} 1 & 0 \end{bmatrix}^\intercal$ or $\begin{bmatrix} 0 & 1 \end{bmatrix}^\intercal$ for the two different orientations of the transmit antennas. Then we can get the four measurements obtained with four transmit-receive antenna orientation configurations in the following way

$$\begin{cases} E_{\theta\theta}^s\left(\mathbf{x}^R,\mathbf{x}^T,\omega\right) = S(\omega)\displaystyle\int_{V(\mathbf{x}^c)} \hat{D}_{11}\chi\left(\mathbf{x}^c\right)\mathrm{d}\, V \\ E_{\theta_\perp\theta}^s\left(\mathbf{x}^R,\mathbf{x}^T,\omega\right) = S(\omega)\displaystyle\int_{V(\mathbf{x}^c)} \hat{D}_{12}\chi\left(\mathbf{x}^c\right)\mathrm{d}\, V \\ E_{\theta\theta_\perp}^s\left(\mathbf{x}^R,\mathbf{x}^T,\omega\right) = S(\omega)\displaystyle\int_{V(\mathbf{x}^c)} \hat{D}_{21}\chi\left(\mathbf{x}^c\right)\mathrm{d}\, V \\ E_{\theta_\perp\theta_\perp}^s\left(\mathbf{x}^R,\mathbf{x}^T,\omega\right) = S(\omega)\displaystyle\int_{V(\mathbf{x}^c)} \hat{D}_{22}\chi\left(\mathbf{x}^c\right)\mathrm{d}\, V \end{cases} \tag{14}$$

Applying (1) and (13) to (14), we can arrive at

$$\begin{cases} E_{\theta\theta}^s\left(\mathbf{x}^R,\mathbf{x}^T,\omega\right) = \cos^2\theta\cdot E_{11} - \sin\theta\cos\theta\cdot E_{21} \\ \qquad -\sin\theta\cos\theta\cdot E_{12} + \sin^2\theta\cdot E_{22} \\ E_{\theta_\perp\theta}^s\left(\mathbf{x}^R,\mathbf{x}^T,\omega\right) = \sin\theta\cos\theta\cdot E_{11} - \sin^2\theta\cdot E_{21} \\ \qquad +\cos^2\theta\cdot E_{12} - \sin\theta\cos\theta\cdot E_{22} \\ E_{\theta\theta_\perp}^s\left(\mathbf{x}^R,\mathbf{x}^T,\omega\right) = \sin\theta\cos\theta\cdot E_{11} + \cos^2\theta\cdot E_{21} \\ \qquad -\sin^2\theta\cdot E_{12} - \sin\theta\cos\theta\cdot E_{22} \\ E_{\theta_\perp\theta_\perp}^s\left(\mathbf{x}^R,\mathbf{x}^T,\omega\right) = \sin^2\theta\cdot E_{11} + \sin\theta\cos\theta\cdot E_{21} \\ \qquad +\sin\theta\cos\theta\cdot E_{12} + \cos^2\theta\cdot E_{22} \end{cases} \tag{15}$$

As in the monostatic configuration $E_{21} = E_{12}$, (15) can be further simplified as

$$\begin{cases} E_{\theta\theta}^s\left(\mathbf{x}^R,\mathbf{x}^T,\omega\right) = E_{11}\cos^2\theta - E_{12}\sin 2\theta + E_{22}\sin^2\theta \\ E_{\theta_\perp\theta}^s\left(\mathbf{x}^R,\mathbf{x}^T,\omega\right) = \dfrac{(E_{11}-E_{22})}{2}\sin 2\theta + E_{12}\cos 2\theta \\ E_{\theta\theta_\perp}^s\left(\mathbf{x}^R,\mathbf{x}^T,\omega\right) = \dfrac{(E_{11}-E_{22})}{2}\sin 2\theta + E_{12}\cos 2\theta \\ E_{\theta_\perp\theta_\perp}^s\left(\mathbf{x}^R,\mathbf{x}^T,\omega\right) = E_{11}\sin^2\theta + E_{12}\sin 2\theta + E_{22}\cos^2\theta \end{cases} \tag{16}$$

In the expressions, $E^s_{\theta_\perp\theta}$ equals to $E^s_{\theta\theta_\perp}$, which agrees with the reciprocity theorem. Another fact that we can observe is that the measurement $E^s_{\theta\theta}$ should be obtained by turning 90 (or 270) in clockwise the orientations of the transmit-receive antennas for $E^s_{\theta_\perp\theta_\perp}$. This can be demonstrated by replacing θ in the last line of (16) with $\theta + 90^\circ$ (or $\theta + 270^\circ$) such that the first line in (16) is arrived. It shows the self-consistency of the derivation.

The relations shown in (16) provide us insight to design a new approach to full polarimetric imaging with differently oriented antenna configurations. Here we focus on the equation in the first line of (16). It shows that the θ co-polarized scattered waves, which are acquired with transmit and receive antennas with orientations of θ from the x_1 axis, contain both the co-polarized (i.e., E_{11} and E_{22}) and cross-polarized (i.e., E_{12}) information that are measured by b_1 or b_2-polarized antennas. Therefore, to extract or reconstruct the full-polarimetric information of targets, one alternative approach is to acquire three co-polarized measurements with antennas of three different orientations. Then application of the relation in (16) helps to reconstruct the full-polarimetric scattering signals that could be observed by b_1 or b_2-polarized antennas. For example, we take the three different orientations as θ_1, θ_2 and θ_3 from the x_1 axis, then this approach can be expressed as

$$\begin{cases} E^s_{\theta_1\theta_1}\left(\mathbf{x}^R, \mathbf{x}^T, \omega\right) = \cos^2\theta_1 \cdot E_{11} - \sin 2\theta_1 \cdot E_{12} \\ \qquad\qquad + \sin^2\theta_1 \cdot E_{22} \\ E^s_{\theta_2\theta_2}\left(\mathbf{x}^R, \mathbf{x}^T, \omega\right) = \cos^2\theta_2 \cdot E_{11} - \sin 2\theta_2 \cdot E_{12} \\ \qquad\qquad + \sin^2\theta_2 \cdot E_{22} \\ E^s_{\theta_3\theta_3}\left(\mathbf{x}^R, \mathbf{x}^T, \omega\right) = \cos^2\theta_3 \cdot E_{11} - \sin 2\theta_3 \cdot E_{12} \\ \qquad\qquad + \sin^2\theta_3 \cdot E_{22} \end{cases} \tag{17}$$

which gives the relations of three co-pol measurements with orientations of θ_1, θ_2 and θ_3 with the full-polarimetric measurements E_{11}, E_{12} and E_{22} in the linear b_1/b_2 polarization basis. Solving the system of linear equations in (17) reconstructs the observables E_{11}, E_{12} and E_{22} in the linear b_1/b_2 polarization basis required in the conventional full-polarimetric imaging approaches. Then the reconstructed measurements E_{11}, E_{12} and E_{22} can be processed by employing either the scalar wave based imaging algorithms or the matrix-based inversion algorithm.

IV. Full-polarimetric Imaging Array Design

A. Array topology

In this section, the proposed approach to full-polarimetric imaging is applied to design, as an example, a rotating antenna array which could be utilized in the GPR systems for the TBM applications. We assume the antenna elements are distributed along three radii of several concentric circles. The antennas on each radius are placed with the same orientation but on different radii different angles are formed with respect to the corresponding radii. The radii selection of concentric circles are determined by the sampling criteria and will be discussion in the next section. An example of the rotating array when the three angles formed between antenna axis and the corresponding radius are 0°, 45° and 90° is illustrated in Fig. 1. With the rotation of the circular disc, three co-polarized measurements are acquired when the three antennas on the same circle sequentially pass by one particular spatial sample point. This operation mechanism for the signal acquisition at a point on the y axis is shown in Fig. 2. One may note that polarizations of the three measurements are distinct at different spatial points as the antenna array rotates circularly, which is a unique feature of the rotating array.

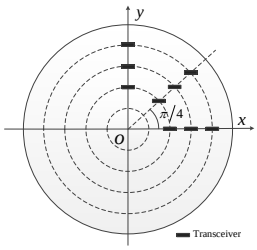

Fig. 1. Topology of the rotating array for full-polarimetric imaging

B. Sampling Criteria

The numbers of antennas along radii and azimuthal samples can be determined based on the polar sampling analysis. To avoid aliasing, it is derived for narrowband (or monochromatic) systems in [25] that regular sampling is performed along the radii and equi-arc-length sampling in the azimuthal direction. The azimuthal sampling spacing is

$$\Delta\varphi = 2\pi/(2N+1), \qquad N = \lceil K_a r \rceil \tag{18}$$

where K_a is the maximum wavenumber related to the scenario, r denotes the radius and N is the smallest integer larger than or equal to $K_a r$. The radial sampling constraint can be obtained in a similar way to the linear arrays. Based on the Nyquist criteria, it should satisfies

$$\Delta r \leqslant \lambda\sqrt{\left(R_a + a\right)^2 + R_0^2}\Big/\left[4\left(R_a + a\right)\right] \tag{19}$$

where λ is the wavelength of the highest frequency of the signal, R_a is the radius of the antenna aperture, R_0 is the distance from target to antenna aperture, a is the radius of the smallest sphere circumscribing the object. As for typical imaging systems the values of the radius of the antenna aperture, the extension of the object and the distance between antenna aperture and the object are comparable, the radial sampling interval is on the order of $\lambda/2$.

In addition, we have to mention that combining ultrawideband (UWB) techniques these constraints could be loosed to take sparse measurements without causing aliasing, especially when the fractional bandwidth is larger than 100%. This is due to the limited interference region of UWB pulses in the space domain [6]. To design a particular sparse sampling strategy for UWB systems involves the spatial sampling (or antenna array) optimization, which is out of the scope of this paper. For simplicity, in the following examples and analyses we will use the equal-angular sampling strategy according to Nyquist criterion.

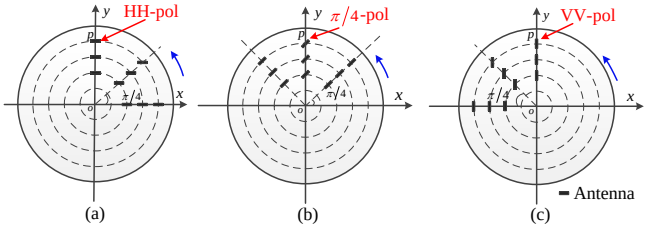

Fig. 2. Operation scheme of the rotating array to acquired three co-pol measurements. (a), (b) and (c) illustrate the three different co-pol measurements at a sampling position on the y-axis acquired sequentially by three antennas on the same circle.

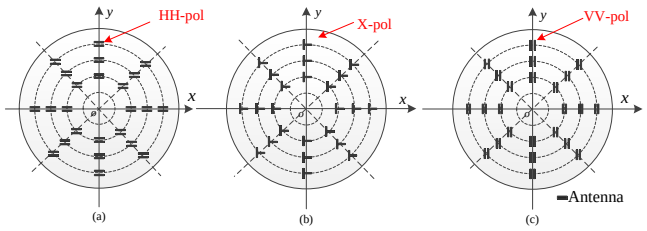

Fig. 3. Topologies of traditional full-polarimetric imaging arrays: (a) HH copol array, (b) HV cross-pol array, and (c) VV copol array.

V. Numerical Simulation

In this section numerical electromagnetic simulations were performed to demonstrate the effectiveness of the proposed approach to full-polarimetric information retrieve and imaging. The simulation models were implemented with the applied electromagnetic simulation software FEKO in which the Method of Moments (MoM) solver is utilized to solve the integral equations. In the models, Hertz dipoles were used as transmit and receive antennas. The operating signal bandwidth was from 2GHz to 10GHz. For comparison, simulations were carried out for both proposed rotating array (Fig. 1) and its traditional counterpart (Fig. 3) for full-polarimetric reconstruction of objects. Due to the feature of the MoM solver, the simulations were implemented in the frequency domain. The synthetic data were converted to time domain by using the Fast Fourier Transform (FFT) after applying a Hanning window. Then the time domain data were focused using the Kirchhoff migration to obtain the full polarimetric images.

Both the traditional full-polarimetric arrays and rotating array performed the same spatial sampling. The rotating antenna array used in the simulation contained 75 antenna elements which were divided into three groups and distributed on three radii with the intervals of 2cm (i.e., $0.4\lambda_c$, where λ_c is the wavelength of the center frequency). The topology was similar to the array shown in Fig. 1. The azimuthal samples were taken every 4° on each circles. Then it resulted in a circular antenna aperture of radius 0.5m (i.e., $10\lambda_c$). With the same spatial sampling intervals, the simulations were also conducted for the traditional full-polarimetric arrays (Fig. 3).

To evaluate the imaging performance, the Point Spread Functions (PSF) of both traditional and rotating arrays for differently polarized signals are shown in Fig. 4 by focusing the scattered signals from a point-like target (i.e., a small sphere). The polarization effects on the focused patterns are noticeable. For all HH, HV and VV polarized signals, the nearly same PSFs were obtained for both arrays. The sidelobes of PSFs for differently polarized signals are all lower than -25dB. However, slightly stronger sidelobes around the focal point can be seen for HV-pol signals (Fig. 4 (f) and (h)). As the cross-pol radiation pattern does not have main lobe but sidelobes, the cross-pol antenna picks up scattered energy via sidelobes while being offset from a scatterer. Thus, it results in relatively stronger sidelobes of cross-pol PSF compared to that of co-pol components. In addtion, we have to mention that the equal-angle sampling of rotating array causes a non-uniform distribution of the samples in the synthesized aperture where the sampling distance is affected by the radius. The non-uniform distribution of samples inherently introduces a space-tapering and may influence the resolutions of a target. To tackle this effect, the samples were weighted by the effective area (e.g., the areas of Voronoi cells) surrounding them within the aperture in the imaging process. That is to say, smaller weighting factors were imposed on densely sampled region while larger weighting factors were used for relatively sparse samples within the aperture. This technique has been utilized for image formation in all experiments in this paper.

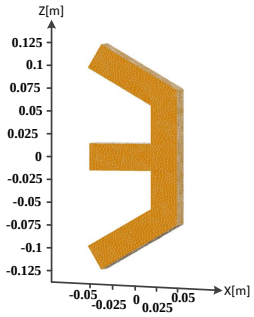

Fig. 5. 'E' shape object used in the simulation

Below numerical simulation was performed for a complex 'E' shape object that was placed in front of the antenna array at a distance of 0.5m (i.e., $10\lambda_c$). The 'E' shape object is illustrated in Fig. 5, which contains a vertical column of the length 15cm, a horizontal bar of the length 10cm in the middle and two inclined bars joined with the vertical column at the two ends. The two inclined bars were 10cm in length and rotated 30° away from the horizontal direction. For all the parts of the 'E' shape object, their width and thickness were 3cm. The synthetic data with rotating array and traditional arrays at 2GHz are shown in Fig. 6. For simplicity of notation, the co-pol measurements of rotating array at each spatial position are defined with respect to the local radius: (1) PP, where the antenna axis is parallel to the radius; (2) NN, where the antenna axis is perpendicular (normal) to the radius, and (3) DD, where the antenna axis forms an angle of 45° with the radius.

A. Full-polarimetric imaging with rotating array and traditional polarimetric arrays

With the help of (17), the polarimetric (i.e., HH, HV(VH), and VV-pol) signals were retrieved from the synthesized PP-,

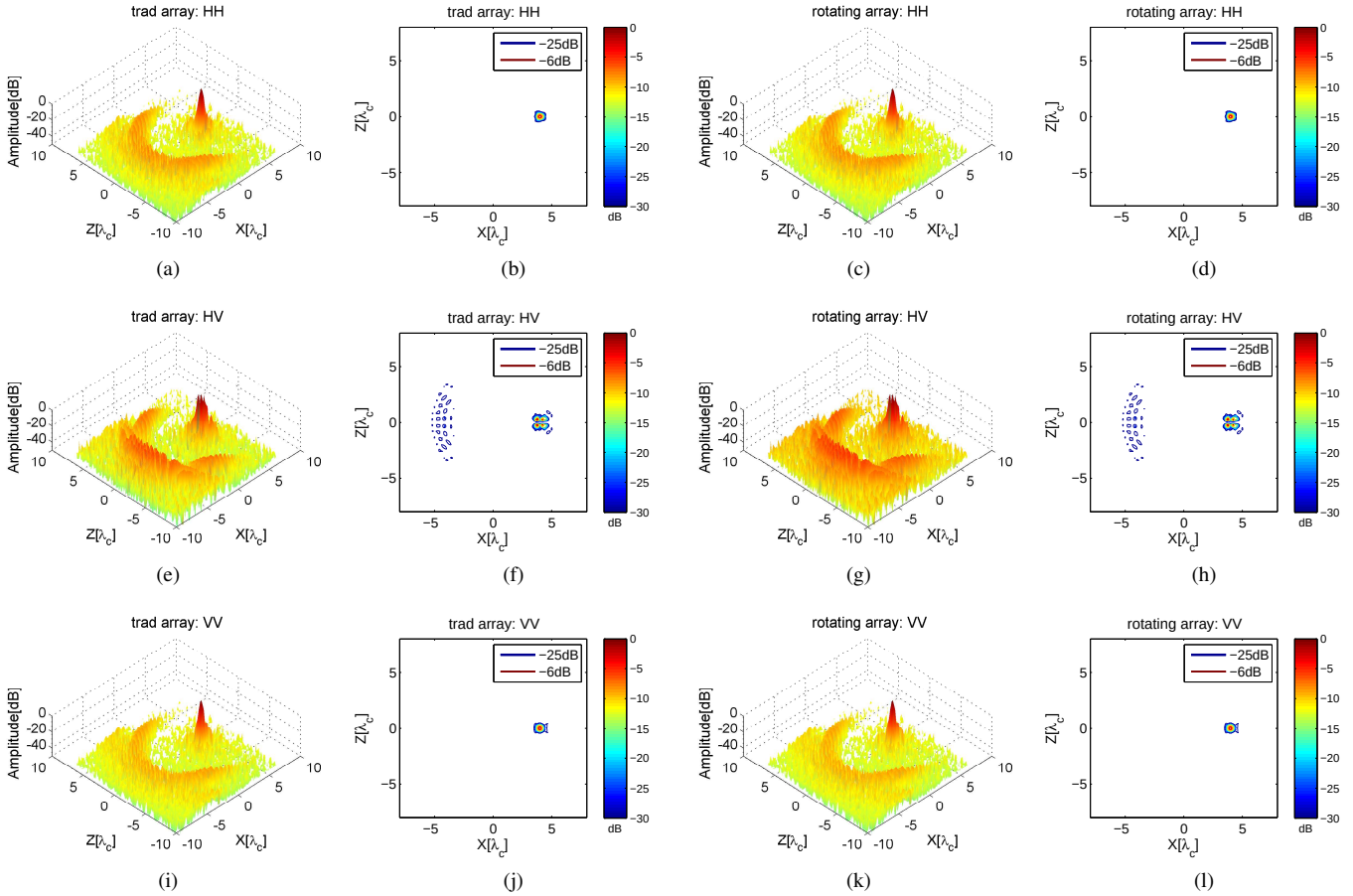

Fig. 4. The normalized focusing patterns of traditional and rotating arrays with focal point at $(4\lambda_c, 10\lambda_c, 0)$ for differently polarized signals. The focusing patterns of traditional array for: (a) HH polarization, (e) HV polarization, (i) VV polarization. (b), (f), and (j) Corresponding contour plots at -25dB beamwidths . The focusing patterns of rotating array for: (c) HH polarization, (g) HV polarization, (k) VV polarization. (d), (h), and (l) Corresponding contour plots at -25dB beamwidths. The ratios between the maximums of focused HH and HV patterns and between the maximums of focused VV and HV patterns are 16.4 and 16.6, respectively.

NN-, and DD-pol signals acquired with the rotating array and denoted as E^{rt}_{HH}, E^{rt}_{HV} and E^{rt}_{VV} in the following. Arbitrarily choosing a spatial sample position, the retrieved polarimetric data $E^{rt}_{HH}, E^{rt}_{HV}$and E^{rt}_{VV} are shown in Fig. 7. Meanwhile, the polarimetric signals E^{m}_{HH}, E^{m}_{HV} and E^{m}_{VV} acquired with traditional array are illustrated as references. The differences of the retrieved polarimetric signals and their corresponding references are also presented (Fig. 7 (b), (d) and (f)). In Fig. 7 (b) and (d), the differences between the retrieved and reference HH and VV signals are approximately 5 orders of magnitude smaller than the reference HH and VV signals. By contrast, the relatively larger differences are observed between the retrieved and reference HV-pol signals but the maximum value of the differences is still not more than 0.5% of the peak amplitude of the reference signal.

To quantitatively analyze the accuracy of the retrieved signals, we introduce the relative error as a metric that is defined as the energy of the differential signal divided by the energy of the reference signal acquired with traditional arrays

$$\alpha = \frac{\sum_{k=0}^{N} \left| E^{rt}\left(t_k\right) - E^{m}\left(t_k\right) \right|^2}{\sum_{i=0}^{N} E^{m}(t_i)^2} \tag{20}$$

where N is the number of discretized samples of the signal. We can see that the smaller the differences between the retrieved signal $E^{rt}\left(t\right)$ and the reference signal $E^{m}\left(t\right)$, the closer α to zero; thus the more accuracy the retrieved signal.

Fig. 8 illustrates the relative errors of the retrieved signals from the corresponding co-pol measurements of antennas on three circles (i.e., R=0.1m, 0.2m and 0.3m) within the synthesized antenna aperture. The considerably small relative errors are observed for the retrieved polarized signals at all the sampling positions (see Fig. 8). However, the relative errors of retrieved HV signals are larger than that of the retrieved co-pol signals. This is due to the fact that the cross-pol signals are actually estimated from the co-pol measurements in the proposed method. This estimation is exactly correct for point-like weak scatterers, and for distributed targets and strong scatterers this estimation is approximate. Nevertheless, the errors of such approximation for cross-pol field reconstruction

are relatively small (about 10^{-5} in Fig. 8 (c)) and their contribution to object imaging is practically negligible.

After imaging operation with Kirchhoff migration [26], the accurately retrieved polarimetric signals lead to almost identical images as that generated by the reference polarimetric signals (Fig. 9). The images formed with both rotating array and traditional arrays reveal the polarization dependence of different parts of the target. For example, the horizontal bar shows higher amplitudes in the HH images while the vertical column is highlighted in the VV images. In the HV images, the inclined bars are well reconstructed and exhibit stronger scattering properties than other parts. The similarities of the corresponding polarimetric images obtained with two approaches can also be quantitatively examined via the relative errors defined in (20) but the time samples of signals are replaced by the voxels of images. The relative errors for the HH, HV and VV images in Fig. 9 are 2.2883×10^{-12}, 6.2041×10^{-6} and 2.1525×10^{-12} in order, which are sufficient to assert identical images are obtained for each polarization.

In addition, comparing the co-pol measurements of rotating array and the signals recorded by traditional arrays in Fig. 6, we can see that the amplitudes of co-pol signals measured with rotating array are relatively uniform and larger than that of cross-polarized signals recorded with traditional array. So considering the same noise level, the rotating array could acquire signals with low susceptibility of noise .

B. Polarimetric imaging VS scalar wave processing

In the proposed antenna array, antennas placed on three radii are required to obtain three different co-polarized measurements at each spatial position for the full-polarimetric signal retrieval and imaging. In practical imaging systems, due to the constraints of cost and system complexity, sometimes only the antennas along single radius can be employed to acquire, for instance, PP- or NN-polarized signals. Then the recorded signals within the antenna aperture are focused like scalar wave to form the image of targets by ignoring the variations of antenna polarizations during the signal acquisition. In this section, we compare the performances of the proposed three co-pol measurements based full-polarimetric imaging, scalar wave imaging with varied polarizations (SWVP for short), scalar wave imaging with aligned polarizations (SWAP for short).

Fig. 10 presents the images reconstructed by PP- and NN-polarized signals with scalar wave processing techniques. To facilitate the comparison, the HH, HV and VV polarimetric images in Fig. 9 are integrated by assigning the backscattering matrices HH, HV and VV directly to red, green and blue components (i.e., Pauli color coding) to obtain a pseudocolor image. For the convenience of visualization, Fig. 11 shows the slices at y=0.5m of the volumetric images obtained by SWAP (i.e., HH and VV), SWVP (i.e., PP, NN) and full-polarimetric imaging. We can see in all the slice images the target shapes are relatively well reconstructed. As expected, in the HH and VV images the horizontal and vertical parts of the targets show higher intensity than the rest. In contrast, SWVP with PP- and NN-polarized signals generate more

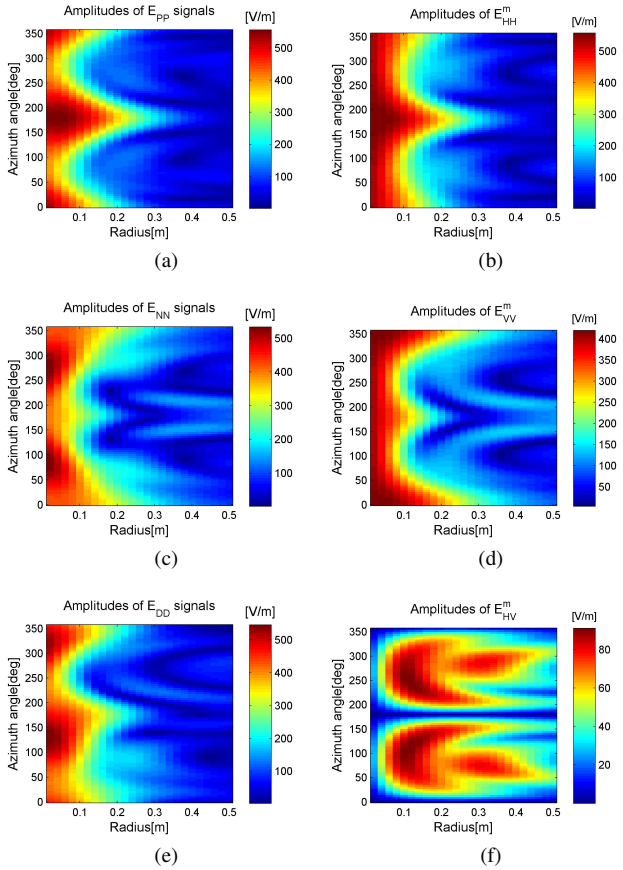

Fig. 6. Amplitudes of the signals measured with rotating array and with traditional polariemtric arrays at $f = 2$GHz: (a), (c) and (e) show the amplitudes of PP-pol, NN-pol and DD-pol measurements in order and (b), (d) and (f) are the amplitudes of HH, VV and HV signals.

uniform images of targets compared to the SWAP images (i.e., HH and VV images) as the PP- or NN-polarized signals contain various information scattered from the different parts of targets. However, more artifacts are observed surrounding the reconstructed target profile in the image of SWVP with NN-polarized signals. Moreover, as HH, HV and VV images are obtained and integrated in the full-polarimetric imaging, so besides the target shapes additional scattering properties of the target can be distinguished from the pseudocolor images, e.g., edge and sharp corner diffraction indicated in green. This can be explained by the fact that the edges and corners cause depolarization of the incident waves and generate strong cross-polarized (HV) backscattered signals. Comparing Fig. 11 (c), (d) and (e), the pseudocolor image is superior to the SWVP images with PP- and NN signals in terms of some details of target structure, specifically, the regions circled by dashed lines in Fig. 11 (c), (d) and (e). The edge of the inclined bar is more clearly formed in the pseudocolor image than the SWVP images (see Fig. 11 (f)-(h)). The same phenomenon can be observed for the edges of the horizontal bar. One can observe that the horizontal bars in the middle and the vertical column are displayed in different colors in Fig. 11 (c) also demonstrates the polarization dependence of their scattering properties. So through different processing and

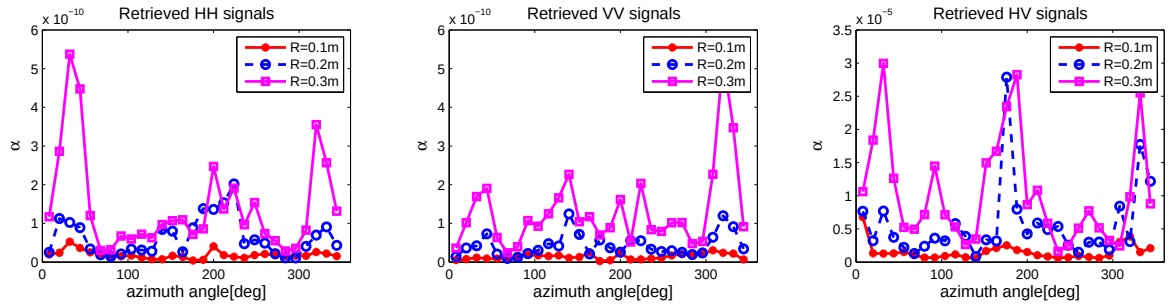

Fig. 8. Relative errors of the retrieved polarimetric signals on three circles (i.e., R=0.1m, 0.2m and 0.3m) within the synthesized antenna aperture. (a) retrieved HH signals; (b) retrieved VV signals and (c) retrieved HV(VH) signals.

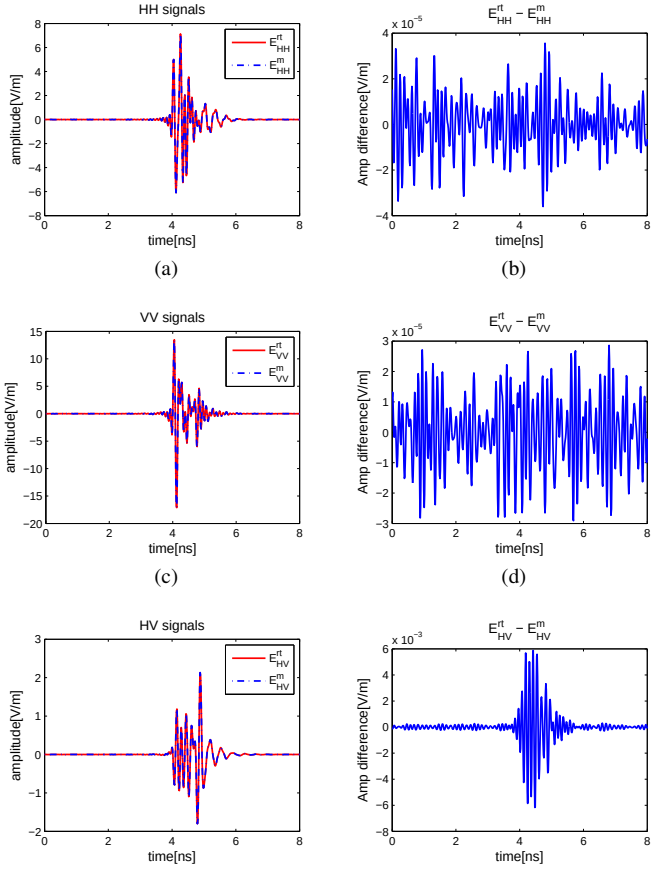

Fig. 7. Comparison of the polarimetric signals (E^m_{HH}, E^m_{VV} and E^m_{HV}) acquired with traditional arrays and the ones (E^{rt}_{HH}, E^{rt}_{VV} and E^{rt}_{HV}) retrieved from the co-pol acquisitions of rotating array. (a), (c) and (e) show the retrieved and measured HH, VV and HV signals, respectively and their differences are presented in (b), (d) and (f).

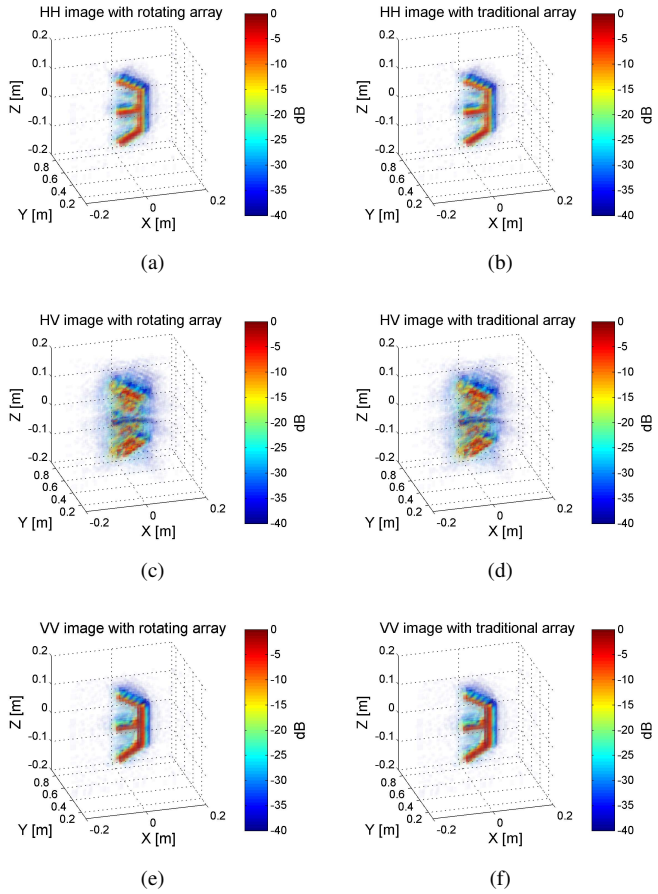

Fig. 9. HH, HV(VH), VV and integrated full polarimetric images obtained with rotating array ((a)(c)(e)) and traditional array ((b)(d)(f)).

visualization techniques, polarimetric images provide various signatures and abundant information for target discrimination and identification compared to the SWAP and SWVP images.

VI. Experimental Results

The aforementioned numerical simulations have shown the effectiveness and accuracy of the proposed approach to full-polarimetric imaging. To further demonstrate its effectiveness, experiments were also performed. The experiment setups for rotating array and traditional polarimetric arrays are illustrated in Fig. 12. To implement the rotating array, a step motor was used to drive a vertical column on top of which a polyethylene plastic panel was mounted to support antennas (Fig. 12 (a)). The step motor was accurately controlled by a computer for positioning and rotating the column. At each spatial sampling position, two anti-podal Vivaldi antennas [30] were used: one for transmission and the other for receiving, see Fig. 12 (c). To reduce the coupling between transmit and

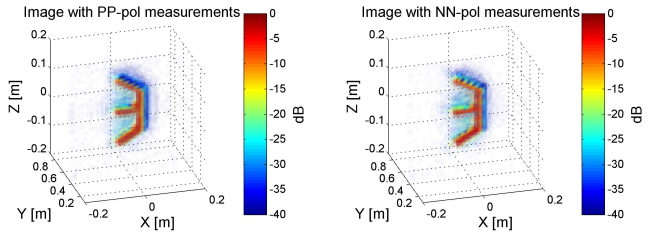

Fig. 10. Images obtained with scalar wave processing for: (a) measurements acquired with antennas of polarizations parallel to the radius (PP-pol); (b) measurements acquired with antennas of polarizations normal to the radius (NN-pol).

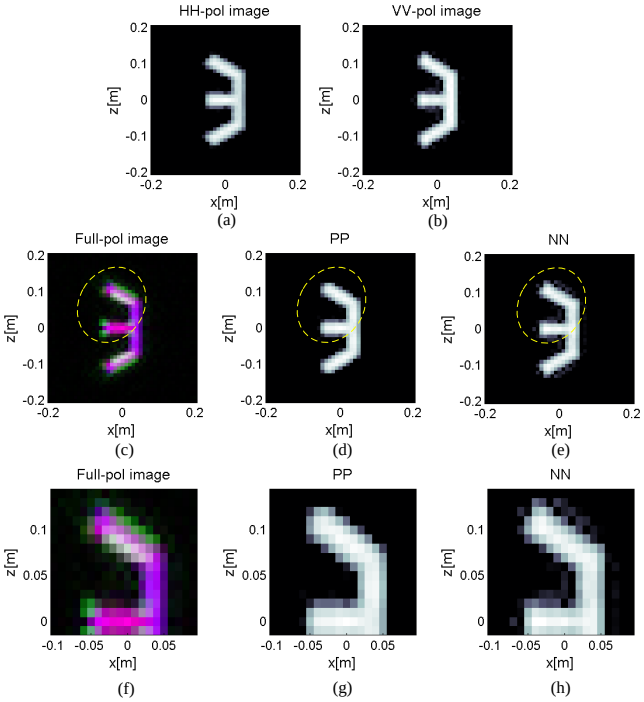

Fig. 11. Slices of the reconstructed volumetric image at y=0.5m by full-polarimetric imaging and scalar wave imaging. (a) and (b) are the slices of HH, VV images with traditional arrays; (c) is the slice of integrated polarimetric image obtained with proposed approach; (d) and (e) are the slices of scalar wave image with PP- and NN-polarized signals, respectively; (f), (g) and (h) are in order the close-ups of the areas indicated by ellipses in (c), (d) and (e).

receive antennas, two antennas were separated by a distance of 6cm. The antennas were connected to a network analyzer and the data were measured in the frequency domain by sweeping the frequencies from 3GHz to 15GHz with a frequency step of 20MHz. Through the shift and rotation of the vertical column, the antennas measured the data on 8 circles of radius ranging from 11cm to 53cm with a step size of 6cm (i.e., $1.8\lambda_c$) and the azimuth sampling interval $d\theta$ on each circle was 1.2 degree. So a planar circular array of radius 0.53m (i.e., $15.9\lambda_c$) was synthesized. A 'L' shape distributed target was placed at a distance of 0.6m (i.e., $15.9\lambda_c$) in front of the center of the equivalent circular array for the test (Fig. 12 (d)). Arranging antennas with orientations along the radius, normal to the radius and 45° with respect to the radius and repeating the measurements over the same sampling grid, then three co-polarized signals, i.e., PP-, NN- and DD-polarized signals were acquired at each sampling position.

For comparison, the reference signals were also measured by the traditional polarimetric arrays over the same sampling grid to acquire HH-, HV- and VV-polarized signals, which was implemented with the planar scanner (Fig. 12 (b)). The signals scattered from the background were also measured in both array cases in the absent of target. Applying the Hanning window to all the signals measured in the frequency domain and taking the inverse Fourier transform, the scattered signals in the time domain were obtained.

After background subtraction, the scattered signals from targets were extracted. The HH-, HV- and VV- signals were retrieved from the PP-, NN- and DD-polarized signals acquired with rotating array by using (17). As an example, the retrieved signals at $(R, \theta) = (0.29\text{m}, -169.2^\circ)$ as well as the corresponding reference signals are shown in Fig. 13. Although background subtraction was taken, some coupling remains are still noticable in all three polarimetric components. In terms of wavelet, relatively good agreement is observed between the retrieved and the reference HH, HV and VV-polarized signals. Focusing both the retrieved and reference polarized signals, the reconstructed polarimetric images are presented in Fig. 14. It can be seen that in both cases the major features of the target are well reconstructed. The corresponding polarimetric images are in good agreement. As for the numerical simulation, the polarization dependence of the horizontal and vertical part of 'L' shape target is clearly visible in the HH- and VV-polarized images, respectively. Meanwhile, the edges of the target can be perceived in the HV images.

However, some discrepancies are observed between the amplitudes of the retrieved and reference signals in Fig. 13 as well as between the images in Fig. 14. In particular, relatively larger discrepancies between the cross-pol images for traditional array and rotating array are seen compared to that between the co-pol images. This can be explained via the estimation errors of cross-pol signals for distributed targets and strong scatterers. In terms of the experiment, the fact that the data were measured with slightly separated transmitting and receiving antennas, i.e., bistatic configuration instead of monostatic one as assumed in the theory derivation might also bring some estimation errors between the results for traditiona array and rotating array. Moreover, large discrepancy between the cross-pol images in the experimental results (Fig. 14 (c) and (d)) might be additionally induced by the non-purity of the linear polarization of anti-podal Vivaldi antenna, especially for high frequencies. In addition, some measurement errors and noise could also lead to some discrepancies between the images obtained with traditional array and rotating array.

To clearly illustrate different polarization features of images in Fig. 14, the color-coded slice images at the target position are shown in Fig. 15. The horizontal and vertical bars are display in red and pink while the edges of the targets are represented in green where the depolarization effect induces the HV polarized signals. Although relatively large differences are observed in the cross-polarized features (Fig. 15 (a) and (b)), rotating array provides comparable imaging performance

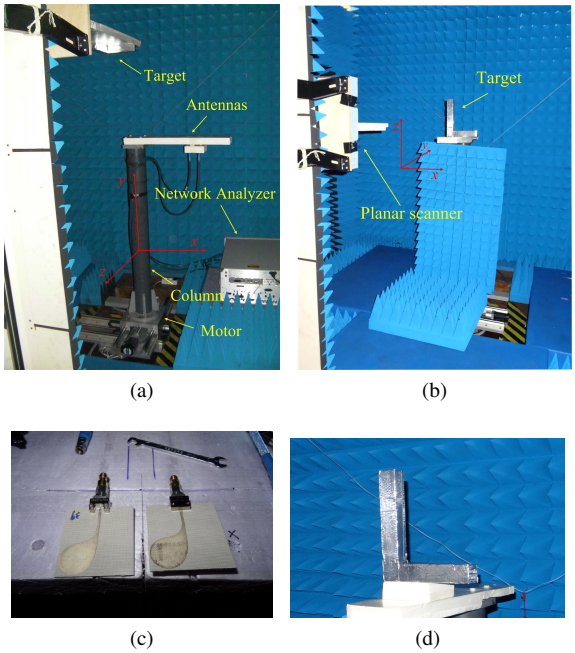

Fig. 12. The experimental setups for rotating array and traditional planar arrays. (a) is the setup for rotating array and (b) for planar array. (c) is the employed anti-podal Vivaldi antennas and (d) is the 'L' shape object.

as the traditional polarimetric arrays.

VII. Conclusion

Full-polarimetric imaging by exploiting the vector nature of the electromagnetic waves provides abundant information for target discrimination and identification. To acquire the full-polarimetric signals for 3-D short-range imaging with rotating antenna arrays within which the antenna polarization changes during the rotation, transformation of polarimetric basis is needed. To this end, we have developed a model in the Born approximation of the scattering process for a pair of transmit and receive antennas with varied polarizations caused by, for example, rotation. The formulation reveals that the acquired signals in a varied polarization basis can always be written as a linear combination of the full-polarimetric signals measured in a fixed polarization basis. That is, the full polarimetric radar signals in a fixed polarization basis, for instance, linear H/V polarization basis, can be retrieved from the signals acquired in different polarization bases.

Taking advantage of the relations derived for the scattered signals in different polarization bases in the modelling, we have proposed an approach to full-polarimetric imaging by acquiring three different co-polarized signals at each sampling position within the aperture. According to this idea, rotating array design for full-polarimetric imaging was given as an example. It can also be extended to rectilinear array design.

Numerical simulations and experimental study for the full-polarimetric imaging performance of rotating array have also be performed to compare it with the traditional polarimetric imaging arrays in the signal and image aspects. The numerical study shows that the full-polarimetric (i.e., HH, VV and HV) signals can be accurately retrieved from the three co-polarized

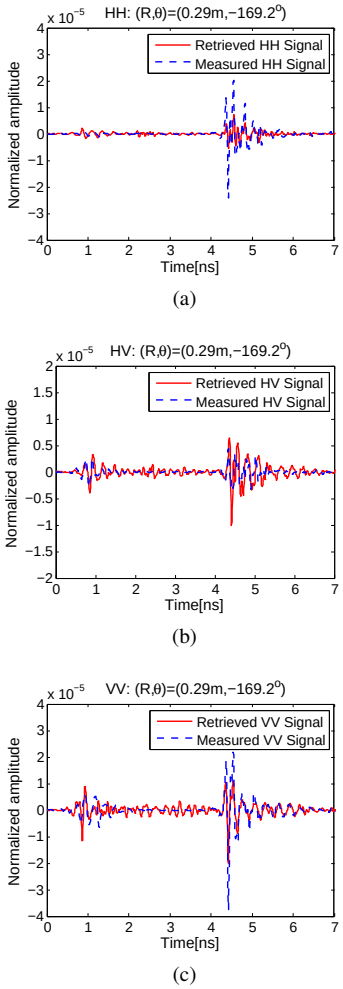

Fig. 13. Comparison of the retrieved polarimetric signals and the reference ones at the position $(R, \theta) = (0.29m, -169.2^\circ)$. (a) HH-polarized signals, (b)HV-polarized signals and (c) VV-polarized signals. The scattered signal spectrum was normalized with respect to the transmitted one.

measurements of the rotating array with the l_2 relative error on the level of 10^{-5} or even smaller compared to the reference signals acquired with traditional polarimetric imaging arrays, thus leading to identical reconstructed volumetric images in short-range applications. Moreover, the imaging results of rotating array obtained by full-polarimetric imaging approach and scalar wave approach (i.e., considering the variation of antenna polarizations within the aperture or not) are compared. Although both approaches are able to reconstruct comparable images of the target shape, the polarimetric imaging by tackling the polarization variation of rotating array reconstructs the edges of target more clearly and reveals more details of the target scattering properties, for instance, the depolarization effect happened at the edges and sharp corners. So it provides extra benefits for target discrimination and identification. The experimental results also demonstrate the effectiveness and accuracy of the proposed approach for full-polarimetric imaging. As in both numerical simulations and experiments linear arrays are used to synthesize circular arrays for demonstration, these may not be the optimal arrays for practical imaging systems. In the next step, we will optimize the array topologies by

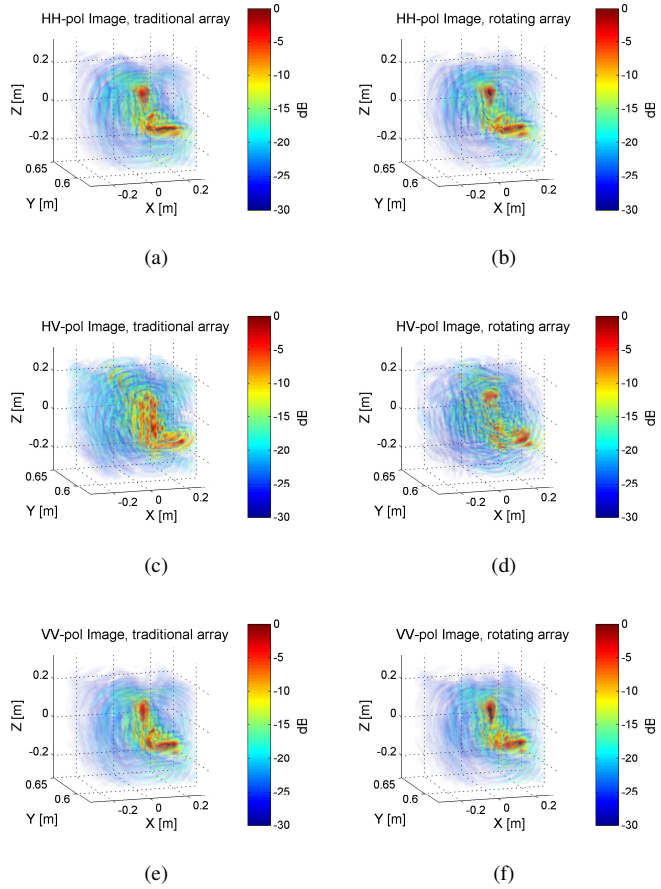

Fig. 14. The polarimetric images obtained with: (a)(c)(e) traditional array; (b)(d)(f) rotating array

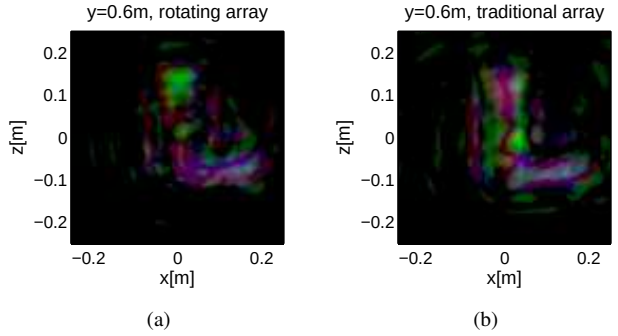

Fig. 15. Pseudocolor slice images at the target position obtained with (a) rotating array and (b) traditional array with dynamic range of 17dB. Pauli color coding is used for visualiztion (HH: Red; HV: Green and VV:Blue).

accounting for the effect of signal bandwidth as well as some practical constraints of the polarimetric imaging systems.

ACKNOWLEDGMENT

The authors would like to thank anonymous reviewers and Prof M. Sato from Tohoku University, Japan for their comments which have helped to improve the manuscript.

REFERENCES

[1] J.-S. Lee and E. Pottier, *Polarimetric radar imaging: from basics to applications*. CRC press, 2009.

[2] D. Daniels, *Ground Penetrating Radar, 2nd Edition*. Institution of Engineering and Technology, 2004.

[3] D. M. Sheen, D. L. McMakin, and T. E. Hall, "Three-dimensional millimeter-wave imaging for concealed weapon detection," *Microwave Theory and Techniques, IEEE Transactions on*, vol. 49, no. 9, pp. 1581–1592, 2001.

[4] X. Zhuge and A. G. Yarovoy, "A sparse aperture mimo-sar-based uwb imaging system for concealed weapon detection," *Geoscience and Remote Sensing, IEEE Transactions on*, vol. 49, no. 1, pp. 509–518, 2011.

[5] A. Abubakar, P. M. van den Berg, and J. J. Mallorqui, "Imaging of biomedical data using a multiplicative regularized contrast source inversion method," *Microwave Theory and Techniques, IEEE Transactions on*, vol. 50, no. 7, pp. 1761–1771, 2002.

[6] J. L. Schwartz and B. D. Steinberg, "Ultrasparse, ultrawideband arrays," *Ultrasonics, Ferroelectrics and Frequency Control, IEEE Transactions on*, vol. 45, no. 2, pp. 376–393, 1998.

[7] D. Velotto, F. Nunziata, M. Migliaccio, and S. Lehner, "Dual-polarimetric terrasar-x sar data for target at sea observation," *Geoscience and Remote Sensing Letters, IEEE*, vol. 10, no. 5, pp. 1114–1118, 2013.

[8] C. Freitas, L. Soler, S. J. S. Sant'Anna, L. V. Dutra, J. R. dos Santos, J. C. Mura, and A. H. Correia, "Land use and land cover mapping in the brazilian amazon using polarimetric airborne p-band sar data," *Geoscience and Remote Sensing, IEEE Transactions on*, vol. 46, no. 10, pp. 2956–2970, 2008.

[9] R. K. Amineh, A. Khalatpour, and N. K. Nikolova, "Three-dimensional microwave holographic imaging using co- and cross-polarized data," *Antennas and Propagation, IEEE Transactions on*, vol. 60, no. 7, pp. 3526–3531, 2012.

[10] Z. Wenji, C. Thajudeen, and A. Hoorfar, "Polarimetric through-the-wall imaging," in *Electromagnetic Theory (EMTS), 2010 URSI International Symposium on*, pp. 471–474.

[11] R. Streich and J. van der Kruk, "Accurate imaging of multicomponent gpr data based on exact radiation patterns," *Geoscience and Remote Sensing, IEEE Transactions on*, vol. 45, no. 1, pp. 93–103, 2007.

[12] M. Lualdi and F. Lombardi, "Orthogonal polarization approach for three dimensional georadar surveys," *NDT & E International*, vol. 60, no. 0, pp. 87–99, 2013.

[13] F. Lehmann, D. E. Boerner, K. Holliger, and A. G. Green, "Multicomponent georadar data: Some important implications for data acquisition and processing," *GEOPHYSICS*, vol. 65, no. 5, pp. 1542–1552, 2000.

[14] U. Boniger and J. Tronicke, "Subsurface utility extraction and characterization: Combining gpr symmetry and polarization attributes," *Geoscience and Remote Sensing, IEEE Transactions on*, vol. 50, no. 3, pp. 736–746, 2012.

[15] R. Salman, I. Willms, L. Reichardt, T. Zwick, and W. Wiesbeck, "On polarization diversity gain in short range uwb-radar object imaging," in *Ultra-Wideband (ICUWB), 2012 IEEE International Conference on*, pp. 402–406.

[16] J. Kruk, C. Wapenaar, J. Fokkema, and P. van den Berg, "Three-dimensional imaging of multicomponent ground penetrating radar data," *GEOPHYSICS*, vol. 68, no. 4, pp. 1241–1254, 2003.

[17] A. Yarovoy, L. Ligthart, A. Schukin, and I. Kaploun, "Polarimetric video impulse radar for landmine detection," *Subsurface Sensing Technologies and Applications*, vol. 3, no. 4, pp. 271–293, 2002.

[18] A. Yarovoy, F. Roth, V. Kovalenko, and L. Ligthart, *Application of UWB Near-Field Polarimetry to Classification of GPR Targets*. Springer New York, 2007, ch. 70, pp. 655–664.

[19] Z. Zeng, J. Li, L. Huang, X. Feng, and F. Liu, "Improving target detection accuracy based on multipolarization mimo gpr," *Geoscience and Remote Sensing, IEEE Transactions on*, vol. PP, no. 99, pp. 1–10, 2014.

[20] J. C. Souyris, P. Imbo, R. Fjortoft, M. Sandra, and J.-S. Lee, "Compact polarimetry based on symmetry properties of geophysical media: the pi/4 mode," *Geoscience and Remote Sensing, IEEE Transactions on*, vol. 43, no. 3, pp. 634–646, 2005.

[21] R. K. Raney, "Hybrid-polarity sar architecture," *Geoscience and Remote Sensing, IEEE Transactions on*, vol. 45, no. 11, pp. 3397–3404, 2007.

[22] E. Torlaschi and Y. Gingras, "Alternate transmission of +45 and 45 slant polarization and simultaneous reception of vertical and horizontal polarization for precipitation measurement," *Journal of Atmospheric and Oceanic Technology*, vol. 17, no. 8, pp. 1066–1076, 2000.

[23] J. Wang, H. Cetinkaya, A. Yarovoy, I. I. Vermesan, and S. Reynaud, "Investigation of forward-looking synthetic circular array for subsurface imaging in tunnel boring machine application," in *Advanced Ground Penetrating Radar (IWAGPR), 2015 8th International Workshop on*, pp. 1–4.
[24] T. Sato, K. Takeda, T. Nagamatsu, T. Wakayama, I. Kimura, and T. Shinbo, "Automatic signal processing of front monitor radar for tunneling machines," *Geoscience and Remote Sensing, IEEE Transactions on*, vol. 35, no. 2, pp. 354–359, 1997.
[25] J. Wang, H. Cetinkaya, and A. Yarovoy, "On polar sampling of gpr for tunneling boring machine," in *Ground Penetrating Radar (GPR), 2014 15th International Conference on*, pp. 330–333.
[26] J. Wiggins, "Kirchhoff integral extrapolation and migration of nonplanar data," *GEOPHYSICS*, vol. 49, no. 8, pp. 1239–1248, 1984.
[27] J. M. Lopez-Sanchez and J. Fortuny-Guasch, "3-d radar imaging using range migration techniques," *Antennas and Propagation, IEEE Transactions on*, vol. 48, no. 5, pp. 728–737, 2000.
[28] Z. Li, J. Wang, J. Wu, and Q. H. Liu, "A fast radial scanned near-field 3-d sar imaging system and the reconstruction method," *Geoscience and Remote Sensing, IEEE Transactions on*, vol. 53, no. 3, pp. 1355–1363, 2015.
[29] S. Zhu, W. Jian, L. Yu, S. Yi, and M. Sato, "A circular measurement for linearly polarized ground penetrating radar to map subsurface crossing cylinders," in *Geoscience and Remote Sensing Symposium (IGARSS), 2013 IEEE International*, pp. 1426–1429.
[30] X. Zhuge and A. Yarovoy, "Design of low profile antipodal vivaldi antenna for ultra-wideband near-field imaging," in *Antennas and Propagation (EuCAP), 2010 Proceedings of the Fourth European Conference on*, pp. 1–5.

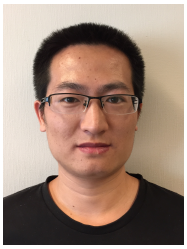

Jianping Wang received BSc. degree from North China University of Technology in 2009 and MSc. degree from Beijing Institute of Technology, Beijing, China, in 2012, both in electrical engineering.

From August, 2012 till April, 2013, he worked as a research associate in the University of New South Wales (UNSW), Australia, on FMCW SAR signal processing for formation flying satellites. In 2013, He joined the group of Microwave Sensing, Signals and Systems (MS3) in the Delft University of Technology, Delft, the Netherlands, where he is working towards the PhD degree. His research interests include Ultra-Wideband (UWB) imaging, signal processing, and antenna array design.

Pascal Aubry received the D.E.S.S. degree in electronics and automatics from the Universit Pierre et Marie Curie (Paris 6), Paris, France, in 1993.

He was a Young Graduate Trainee with the European Space Research and Technology Centre (ESTEC) in 1996, where he was involved in antenna measurements. Since 1997, he has been with the International Research Centre for Telecommunications and Radar, Delft University of Technology (TUD), Delft, The Netherlands. His research interests include antenna measurement techniques, radar system testing, and signal processing and analysis.

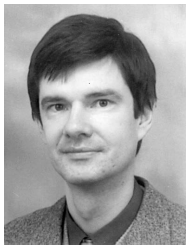

Alexander Yarovoy (F'15) received the Diploma (with honor) in radiophysics and electronics in 1984, and the Candidate Phys. & Math. Sci. and Doctor Phys. & Math. Sci. degrees in radiophysics in 1987 and 1994, respectively, all from the Kharkov State University, Kharkov, Ukraine.

In 1987, he joined the Department of Radiophysics at the Kharkov State University as a Researcher and became a Professor there in 1997. From September 1994 to 1996, he was with the Technical University of Ilmenau, Ilmenau, Germany, as a Visiting Researcher. Since 1999, he has been with the Delft University of Technology, Delft, The Netherlands. Since 2009, he leads there as the Chair of Microwave Sensing, Signals and Systems. His main research interests are in ultrawideband microwave technology and its applications (particularly radars) and applied electromagnetics (particularly UWB antennas). He has authored and coauthored more than 250 scientific or technical papers, four patents, and 14 book chapters.

Prof. Yarovoy served as a Guest Editor of five special issues of the IEEE Transactions and other journals. Since 2011, he has been an Associated Editor of the International Journal of Microwave and Wireless Technologies. He is the recipient of the European Microwave Week Radar Award for the paper that best advances the state of the art in radar technology in 2001 (together with L. P. Ligthart and P. van Genderen) and in 2012 (together with T. Savelyev). In 2010, together with D. Caratelli, he got the best paper award of the Applied Computational Electromagnetic Society (ACES). He served as the Chair and TPC Chair of the 5th European Radar Conference (EuRAD 08), Amsterdam, The Netherlands, as well as the Secretary of the 1st European Radar Conference (EuRAD 04), Amsterdam. He served also as the Cochair and TPC Chair of the Xth International Conference on Ground Penetrating Radar (GPR 2004) in Delft, The Netherlands. Since 2008, he has served as the Director of the European Microwave Association.